J. Eng. Technol. Sci., Vol. 54, No. 4, 2022, 220403

Discretization Corrected Particle Strength Exchange for Steady State Linear Elasticity

Christopher Adnel & Lavi Rizki Zuhal*

Flight Physics Research Group, Faculty of Mechanical and Aerospace Engineering, Institut Teknologi Bandung, Jalan Ganesa No. 10 Bandung 40132, Indonesia
*E-mail: lavirz@ae.itb.ac.id

Highlights:

- The DC PSE method was successfully implemented to solve the Navier-Cauchy equation for linear static elasticity.
- Convergence of DC PSE was proven against empirical and analytical results.
- Most of the computational time in the author's code is attributed to large sparse matrix inversion and the particle neighbor search algorithm.

Abstract. Discretization corrected particle strength exchange (DC PSE) is a particle based spatial differential operator designed to solve meshless continuum mechanics problems. DC PSE is a spatial gradient operator that can discretize a computational domain with randomly distributed particles, provided that each particle has enough neighboring particles. In contrast, conventional methods such as the standard finite difference method require the computational domain to be discretized into a Cartesian grid. In linear elasticity simulations, especially steady state cases, this domain is mostly discretized using mesh-based methods such as finite element. However, while particle methods such as smoothed particle hydrodynamics (SPH) have been widely applied to solve dynamic elasticity problems, they have rarely been used in steady state simulations. In this study, a DC PSE operator was used to solve steady linear elasticity problems in a two-dimensional domain. The result of the DC PSE numerical simulation was compared to numerical results, empirical formula results, and results from conventional commercial finite element software, respectively.

Keywords: *convergence test; DC PSE; elastostatics; linear elasticity; particle method.*

1 Introduction

In continuum mechanics simulations, the computational domain is usually discretized using either a mesh-based method or a particle-based method. Mesh based methods are very widely used and are applied in most commercial simulation software, whereas particle-based methods are much less prevalent in most engineering applications. The popularity of mesh-based methods is due to their efficiency in terms of computational time. Mesh-based methods generally

Received December 6th, 2021, 1st Revision December 28th, 2021, 2nd Revision January 25th, 2021, Accepted for publication February 9th, 2022.
 ISSN: 2337-5779, DOI: 10.5614/j.eng.technol.sci.2022.54.4.3

require a smaller number of elements to simulate a complex shaped domain. However, particle-based methods still have some advantages compared to mesh-based methods, such as reduction of computational time for mesh generation and their high structural deformation capabilities for solid mechanics simulations.

The particle-based methods were pioneered by the development of Smoothed Particle Hydrodynamics (SPH) by Monaghan & Gingold [1]. However, the earliest SPH method was only zeroth-order consistent at best, which led to inaccurate results when solving for higher order equations. Decades have passed since the development of the earliest SPH method and many other particle-based discretization methods have emerged. One of these new particle-based discretization methods is Discretization Corrected Particle Strength Exchange (DC PSE), which can be made consistent up to any arbitrary order. Developed by Schradder in 2011 [2], DC PSE is a corrected particle gradient operator based on the Particle Strength Exchange (PSE) operator developed by Mas-Gallic in 1989 and generalized into an arbitrary differential operator by Eldredge in 2002 [3]. DC PSE employs a correction using a polynomial with arbitrary order, which ensures consistency to that respective order.

The steady state linear elasticity equation to be solved in this paper is a strong formulation in the form of second-order partial differential equations (Navier-Cauchy equations). This governing equation is derived only from the momentum equilibrium, and it assumes the solid to be linearly elastic (small deformations) and incompressible (constant density). Both Neumann (traction) and Dirichlet (displacement) boundary conditions are also applied to model either traction, free, or displacement boundaries. These partial differential equations are discretized using DC PSE to create a system of linear equations, which can then be solved implicitly using methods such as LU decomposition [4]. Regarding the application of DC PSE in solid mechanics, Bourantas, *et al*. applied the DC PSE operator to solve steady state linear equations by combining it with a standard finite difference method in a hybrid formulation [5]. In their method, Bourantas, *et al.* utilize DC PSE for boundary particles, whereas inner particles are solved using finite difference method.

In the present research, DC PSE was applied to the whole simulation domain for consistency and to gauge the accuracy of a complete DC PSE elastostatics simulation. This paper provides the theoretical background of both linear elasticity and the DC PSE operator, as well as several test cases in a two-dimensional domain to benchmark the performance of DC PSE compared to both analytical and conventional finite element results.

2 Theoretical Background

2.1 Linear Elasticity

The special case of the Navier Cauchy equation that governs the steady state linear elasticity equation is derived from the steady state momentum equilibrium in Eq. (1).

$$\nabla . \sigma = -f \tag{1}$$

Hooke's law for the constitutive equation of a linear isotropic elastic material in Eq. (2) is used for the stress-strain relations, where λ and μ are the Lamé constants.

$$\sigma = \lambda . tr(\varepsilon) . I + 2\mu\varepsilon \tag{2}$$

$$\lambda = \frac{v.E}{(1+v)(1-2v)} \tag{3}$$

$$\mu = \frac{E}{2(1+v)} \tag{4}$$

In linear elasticity, the material is limited to small deformations only, where the linear strain-displacement relations in Eq. (5) can be applied.

$$\varepsilon = \frac{1}{2}[\nabla u + (\nabla u)^T] \tag{5}$$

Therefore, in terms of displacement, the Navier Cauchy equation can be written as in Eq. (5) [6, 7].

$$(\lambda + 2\mu)\nabla(\nabla u) + \mu\nabla^2 u = -f \tag{6}$$

For Neumann boundaries (Ω_{N}) where the traction acting on the solid surface is defined, the following equation is used, where n is the boundary surface's outward normal vector and t is the traction vector acting on the boundary surface.

$$\sigma . n = t \tag{7}$$

For Dirichlet boundaries (Ω_{D}) where the displacement is defined, the following equation is used, where d is the defined displacement vector.

$$u = d \tag{8}$$

These boundaries are visualized for an arbitrary shaped domain in Figure 1. In this domain, Eq. (6) is valid for inner particles inside of the domain, denoted by Ω. Eq. (7) is valid for boundary particles where traction load is applied, as well as boundaries with no prescribed load or displacement (traction free boundary). This boundary is denoted by Ω_N, or the Neumann boundary. The last boundary is the prescribed displacement boundary, denoted by Ω_D, or the Dirichlet boundary.

In this boundary, the particle displacement is prescribed (it can be either fixed or displaced to a certain length).

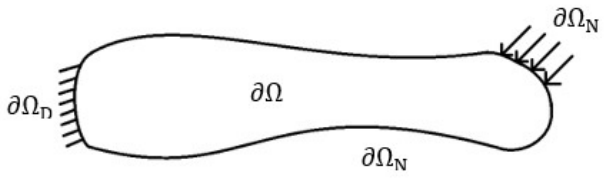

Figure 1 Neumann and Dirichlet boundary visualization.

In a two-dimensional domain, the governing equations can be written as follows:

$$\begin{aligned}(\lambda+2\mu)\frac{\partial^2 u_x}{\partial x^2}+\mu\frac{\partial^2 u_x}{\partial y^2}+(\lambda+\mu)\frac{\partial^2 u_y}{\partial x\partial y}&=-f_x\\(\lambda+2\mu)\frac{\partial^2 u_y}{\partial y^2}+\mu\frac{\partial^2 u_y}{\partial x^2}+(\lambda+\mu)\frac{\partial^2 u_x}{\partial x\partial y}&=-f_y\end{aligned}\qquad \in \Omega \qquad (9)$$

$$\begin{aligned}(\lambda+2\mu)\frac{\partial u_x}{\partial x}n_x+\mu\frac{\partial u_x}{\partial y}n_y+\lambda\frac{\partial u_y}{\partial y}n_x+\mu\frac{\partial u_y}{\partial x}n_y&=t_x\\(\lambda+2\mu)\frac{\partial u_y}{\partial y}n_y+\mu\frac{\partial u_y}{\partial x}n_x+\lambda\frac{\partial u_x}{\partial x}n_y+\mu\frac{\partial u_x}{\partial y}n_x&=t_y\end{aligned}\qquad \in \Omega_N \qquad (10)$$

$$\begin{aligned}u_x&=d_x\\u_y&=d_y\end{aligned}\qquad \in \Omega_D \qquad (11)$$

2.2 DC PSE Operator

The DC PSE gradient operator developed by Schradder [2] is written as follows:

$$Q^m f(x_p)=\frac{1}{\varepsilon(x_p)^{\sum_{i=1}^{n} m_i}}\sum_{x_q\in N(x_p)}\left(f(x_q)\pm f(x_p)\right)\eta\left(\frac{x_p-x_q}{\varepsilon(x_p)}\right) \qquad (12)$$

Q^m	:	spatial gradient approximation at order *m*
m	:	spatial differentiation order at basis *i*
n	:	number of dimensions in Euclidian space
$\varepsilon(x_p)$	:	spatially dependent scaling function
$N(x_p)$	:	neighboring particle set of x_p
$f(x_p)$	:	base function to be differentiated in x_p
$\eta(x)$	:	corrected weighting function

The corrected weighting function $\eta(x)$ is based on a squared exponential kernel/Gaussian kernel, which is corrected using a polynomial of a certain order with p as its monomial basis vector. This correction increases the operator's order

of consistency to the same order. $\eta(x)$ for two-dimensional cases is shown in Eq. (13). To ensure computational efficiency, the particle interaction is also limited only up to a certain cut-off radius, r_c, as visualized in Figure 2.

$$\eta\left(\frac{x_p - x_q}{\varepsilon(x_p)}\right) = \begin{cases} e^{\left(\frac{-\sum_{i=1}^{n}(x_{p_i} - x_{q_i})^2}{\varepsilon(x_p)^2}\right)} . p\left(\frac{x_p - x_q}{\varepsilon(x_p)}\right) . a^T(x_p), \left|\left|x_p - x_q\right|\right| \leq r_c \\ 0 \qquad\qquad , \left|\left|x_p - x_q\right|\right| \geq r_c \end{cases} \tag{13}$$

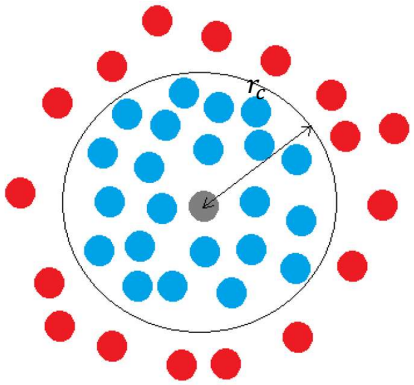

Figure 2 Neighboring particle visualization (blue indicates interaction, red means no interaction, and grey denotes the particle of interest).

From Eq. (13), $p(x_p - x_q).a^T(x)$ is the polynomial correction with $a^T(x)$ as the polynomial constants. The constant $a_{i,j}$ is determined by solving the following matrix equations:

$$A(x_p)a^T(x_p) = b \tag{14}$$

with

$$A(x_p) = B(x_p)^T B(x_p) \tag{15}$$

$$B(x_p) = E(x_p)V(x_p) \tag{16}$$

$$b = (-1)^{\sum_{i=1}^{2} m_i} D^m p(x)|_{x=0}$$

$$V(x_p) = \begin{bmatrix} p_1\left(\frac{z_1(x_p)}{\varepsilon(x_p)}\right) & p_2\left(\frac{z_1(x_p)}{\varepsilon(x_p)}\right) & \cdots & p_l\left(\frac{z_1(x_p)}{\varepsilon(x_p)}\right) \\ p_1\left(\frac{z_2(x_p)}{\varepsilon(x_p)}\right) & p_2\left(\frac{z_2(x_p)}{\varepsilon(x_p)}\right) & \cdots & p_l\left(\frac{z_2(x_p)}{\varepsilon(x_p)}\right) \\ \vdots & \vdots & \ddots & \vdots \\ p_1\left(\frac{z_k(x_p)}{\varepsilon(x_p)}\right) & p_2\left(\frac{z_k(x_p)}{\varepsilon(x_p)}\right) & \cdots & p_l\left(\frac{z_k(x_p)}{\varepsilon(x_p)}\right) \end{bmatrix} \quad (17)$$

$$E(x_p) = diag\left(\left[e^{\frac{|z_q(x_p)|^2}{2\varepsilon^2}}\right]_{q=1}^{k}\right) \quad (18)$$

$$b = (-1)^{\sum_{i=1}^{2} m_i} D^m p(x)|_{x=0} \quad (19)$$

$$z_q(x_p)_{q=1}^{k} = \left(x_p - x_q\right)_{x_q \in N(x_p)} \quad (20)$$

In the equations, $V(x_p)$ is a Vandermonde matrix from the monomial basis $p(z)$, with the subscript l denoting the number of moment conditions that need to be satisfied and k denoting the number of neighboring nodes inside the cut-off radius. For the matrix $A(x_p)$ to have its inverse, it is crucial that the number of neighboring nodes k is higher or equal to the number of moment conditions l. Therefore, the condition $k \geq l$ must be fulfilled. The determination of cut-off radius r_c depends mostly on the minimum number of neighboring particles due to these moment conditions. Increasing r_c above this threshold, however, will not produce any notable improvement to the accuracy of the method because of the exponential kernel in DC PSE, which diminishes the contribution by particles above $r_c > 3h$.

3 Results Validation

In this research, two benchmark problems in two-dimensional domains were simulated: a simple cantilever beam bending case and a traditional hollowed plate stress concentration case.

3.1 Cantilever Beam with Shear Load

The cantilever beam schematic in Figure 3**Error! Reference source not found.** shows a beam with length L and width b, which is fixed on the left and downward distributed shear load W is applied on the other end. The values of L, b, W, and other beam parameters are given in Table 1. In this simulation, the particle spacing was varied between 0.01 m to 0.0025 m (500 to 8,000 particles) to check for convergency of the scheme. The resulting y-axis midpoint displacement comparison between the present work and the analytical Euler beam equation is

shown in Figure 4, which shows good convergency to the analytical solution. The absolute displacement error diminishes with the decrease of particle spacing, as shown in Figure 5.

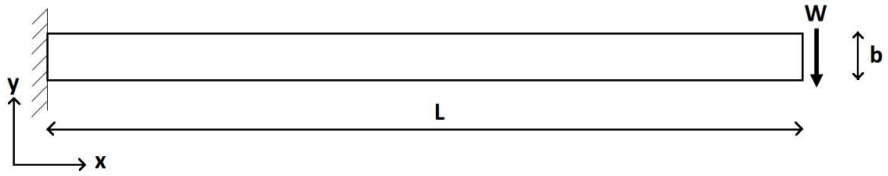

Figure 3 Cantilever beam with shear load test case schematic.

Table 1 Cantilever beam with shear load test case details.

Young's Modulus	200	Gpa
Poisson's Ratio	0.3	
L	1	m
b	0.05	m
Thickness	0.001	m
W	20000	kN/m^2

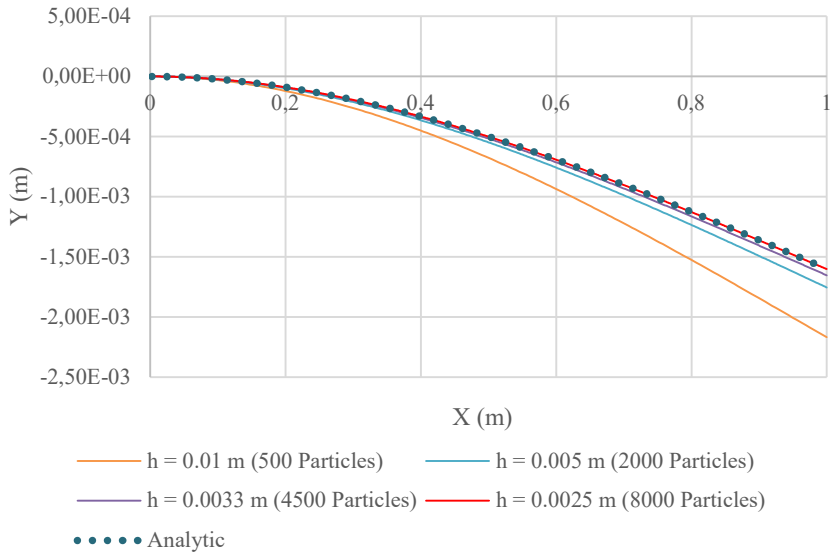

Figure 4 Cantilever beam y-axis deflection plot for various particle spacings.

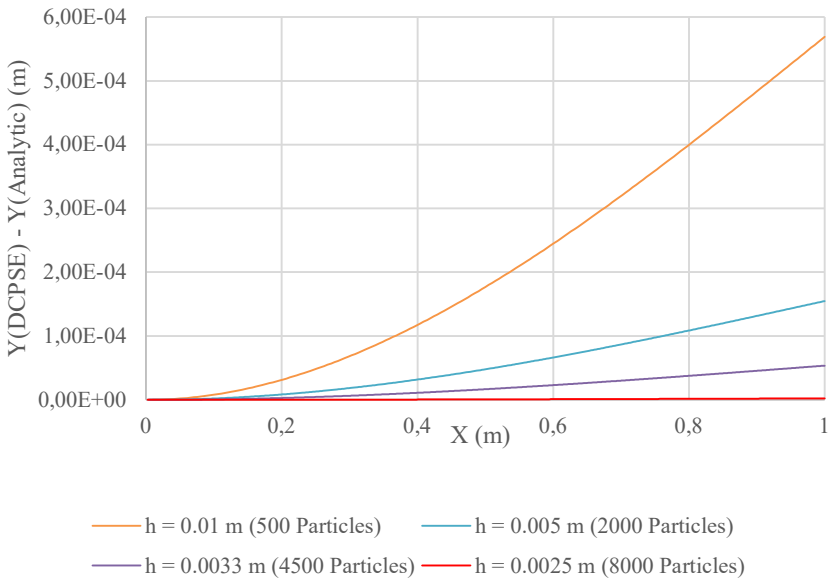

Figure 5 Cantilever beam y-axis deflection error for various particle spacings.

Based on the results, using 8,000 particles results in a tip deflection relative error of 0.14%. The normal stress contour for this benchmark problem using 8,000 particles is shown in Figure 6.

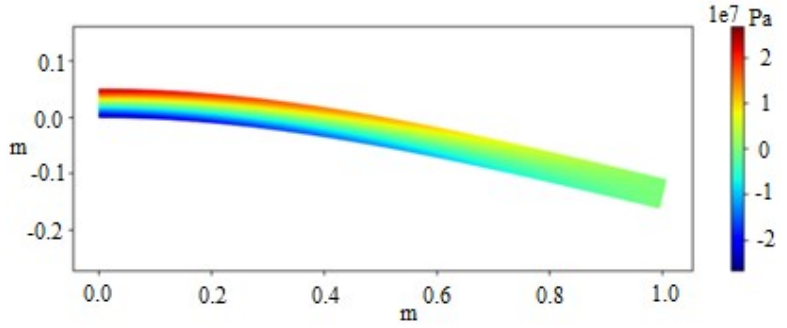

Figure 6 Cantilever beam normal stress contour (8,000 particles, $\delta_{Scale} = 100$).

Regarding the computational time, the computational complexity of the authors' code is approximately $O(N^2)$ due to the naïve neighbor search algorithm as well as the LU decomposition algorithm used. The computational time for various particle numbers for the cantilever beam case is shown in Figure 7.

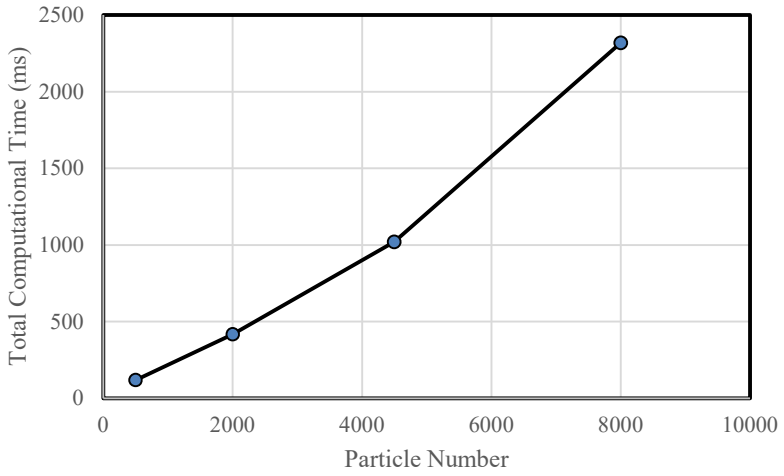

Figure 7 Cantilever beam total computational time for various particle spacings.

3.2 Hollowed Plate with Tensile Load

The hollowed plate schematic in Figure 8 shows that the plate is fixed on the left and normal distributed load W is applied on the other end. The plate dimension (length L, width b, and circular hollow radius R), material properties, and W value are given in Table 2.

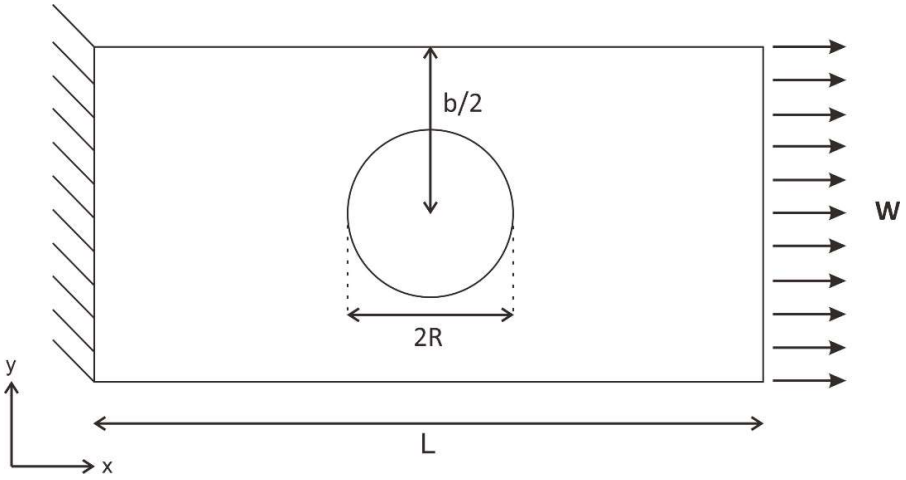

Figure 8 Hollowed plate with tensile load test case schematic.

Table 2 Hollowed plate with tensile load test case details.

Young'' Modulus	200	Gpa
Poisson's Ratio	0.3	
L	0.6	m
b	0.3	m
R	0.075	m
Thickness	0.001	m
W	10000	kN/m^2

For this test case, the particles are distributed through the outer and inner boundary lines to capture the plate's curvature, especially the circular hollow boundary. The inner particles are distributed using a standard Cartesian grid. This particle distribution is shown in Figure 9. It demonstrates the strength of particle methods, where particles can be distributed arbitrarily, provided there are enough neighboring particles for each particle's gradient approximation.

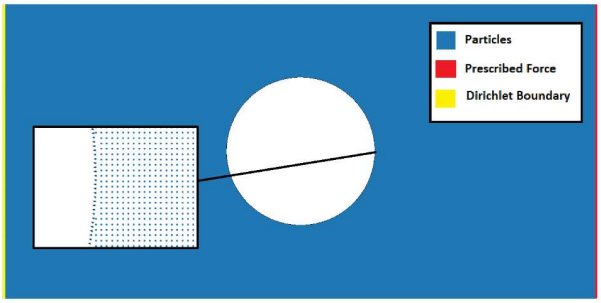

Figure 9 Hollowed plate with tensile load particle distribution.

In this test case, stress concentration occurs on the circular hollow surfaces and the value of the normal stress at that location is used as a comparison between the results present work, commercial FEM software, numerical calculation, and an empirical formula. The empirical formula for the stress concentration is given in Eq. (21) and Eq. (22), where d is the hole diameter, W is the width of the plate perpendicular to the tensile load vector, and σ_∞ is the tensile load acting on the plate [8]. The result of this comparison is detailed in Table 3, which shows good agreement between the results from the present work, commercial FEM software (0.78% difference), and the empirical result (2.2% difference). The overall normal stress contour from the present work also matches the ANSYS simulation result well, as shown in Figure 10.

A convergency test was also conducted for this test case by varying the particle number used in the simulation. The maximum normal stress vs particle number chart in Figure 11 shows that the present DC PSE discretization scheme has good

convergence to the empirical results, with convergence reached at approximately 5,000 particles. Regarding computational efficiency, the effect of particle number increment on computational time for the second test case is shown in Figure 12.

$$K_t = 3 - 3.14\left(\frac{d}{W}\right) + 3.667\left(\frac{d}{W}\right)^2 - 1.527\left(\frac{d}{W}\right)^3 \tag{21}$$

$$\frac{\sigma_{max}}{\sigma_\infty} = K_t \frac{1}{1-\left(\frac{d}{W}\right)} \tag{22}$$

Table 3 Hollowed plate with tensile load simulation results (162733 particles).

$\boldsymbol{\sigma_\infty}$	10,000	kN/m^2
$\boldsymbol{K_t}$ **(Empirical Formula)**	2.1559	
$\boldsymbol{\sigma_{xx\,max}}$ **(Empirical Formula)**	43118	kN/m^2
$\boldsymbol{\sigma_{xx\,max}}$ **(Numerical DC PSE)**	44070	kN/m^2
$\boldsymbol{\sigma_{xx\,max}}$ **(Numerical ANSYS)**	43731	kN/m^2
Relative Error from Empirical	**0.0221**	
Relative Error from ANSYS	**0.0078**	
Particle Number	162,733	
ANSYS Node Number	41,265	
ANSYS Element Number	40,748	

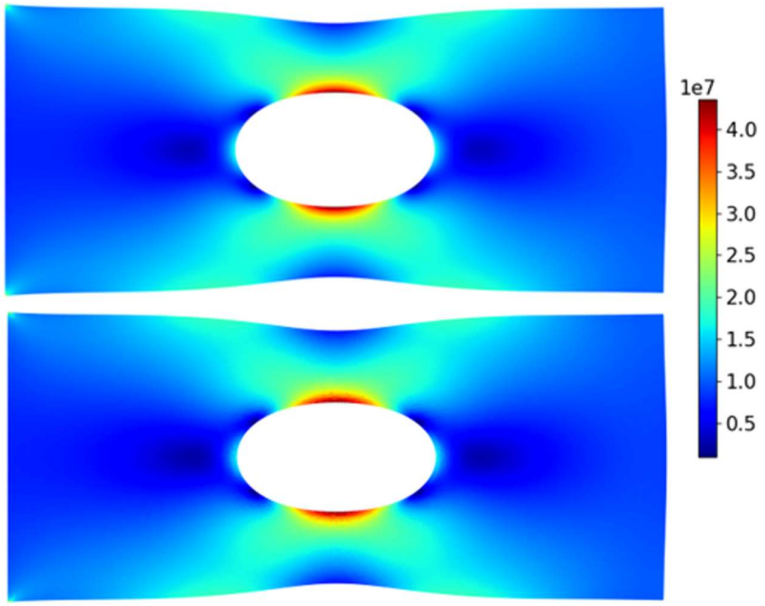

Figure 10 Hollowed plate with tensile load normal stress contour (162,733 particles, top: present work, bottom: ANSYS simulation) ($\delta_{Scale} = 2{,}000$).

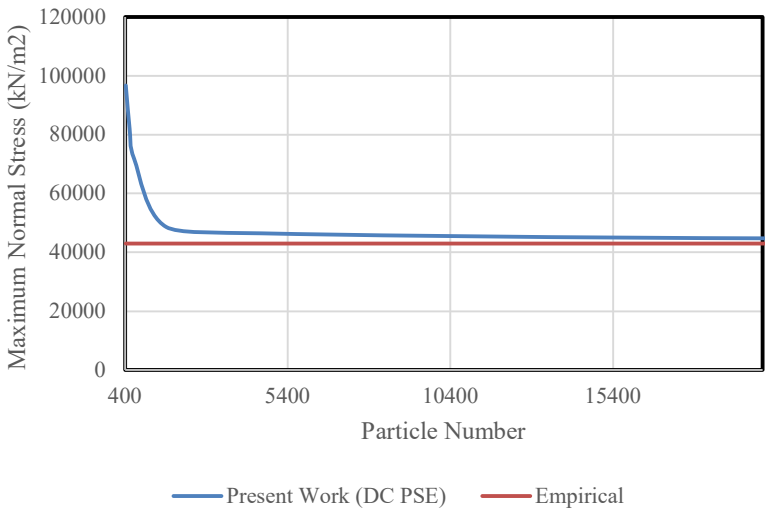

Figure 11 Hollowed plate maximum normal stress convergency plot.

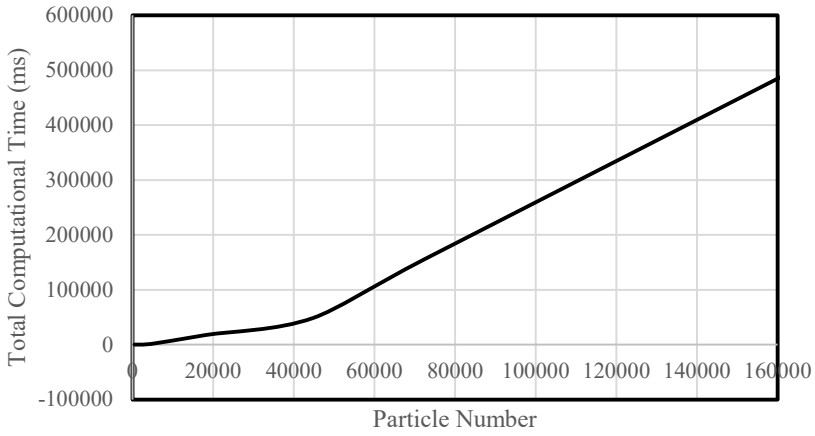

Figure 12 Hollowed plate total computational time for various particle numbers.

4 Conclusion

Based on the DC PSE simulation conducted in the present work, it can be concluded that the DC PSE differential operator is able to achieve high accuracy for steady state linear elasticity problems. All the test cases simulated using DC PSE yielded below 1% relative error compared to either analytical results or commercial finite element software.

However, to achieve this level of accuracy, the present DC PSE formulation requires a much higher number of particles compared to conventional finite element methods, which severely impacts computational efficiency. Fortunately, particle methods such as the present DC PSE formulation do not require a mesh generation algorithm, as the particles can be distributed freely. This was demonstrated by the hollowed plate test case, where the boundary particles can be distributed to follow the boundary shape, while the inner particles can be simply placed on a cartesian grid.

In future works, the authors wish to implement this DC PSE gradient operator to other problems in solid mechanics, such as dynamic elasticity and fracture mechanics. Implementation of DC PSE in fluid structure interaction applications is also a promising field the authors wish to explore

References

[1] Gingold, R.A. & Monaghan, J.J., *Smoothed Particle Hydrodynamics: Theory and Application to Non-Spherical Stars*, Mon. Not. R. Astron. Soc., **181**(3), pp. 375-389, 1997.

[2] Schrader, B., *Discretization-Corrected PSE Operators for Adaptive Multiresolution Particle Methods*, ETH Library, Zürich, 2011.

[3] Eldredge, J.D., Leonard, A. & Colonius, T., *A General Deterministic Treatment of Derivatives in Particle Method*, Journal of Computational Physics, **2**(180), pp. 686-709, 2002.

[4] Bracha-Barak, A., & *A Factorization Procedure for the Solution of Multidimensional Elliptic Partial Differential Equations*, SIAM Journal on Numerical Analysis, **1**(5), pp. 887-893, 1974.

[5] Bourantas, G.C., Mountris, K.A. & Loukopoulos, V., *Strong-form Approach to Elasticity: Hybrid Finite Difference-Meshless Collocation Method (FDMCM)*, Applied Mathematical Modelling, **57**, pp. 316-338, 2018.

[6] Lautrup, B., *Physics of Continuous Matter: Exotic and Everyday Phenomena in the Macroscopic World*, CRC Press, 2011.

[7] Morales, J.L., Moreno, J. & Alhama, F., *Numerical Solutions of 2-D Linear Elastostatic Problems by Network Method*, Computer Modelling in Engineering and Sciences, **76**, pp. 1-18, 2011.

[8] McGinty, Bob, *Fracture Mechanics*, https://www.fracturemechanics.org/hole.html. (17 May 2020)

[9] Gray, J.P., Monaghan, J.J. & Swift, R.P., *SPH Elastic Dynamics*, Computer Methods in Applied Mechanics and Engineering, **190**, pp. 6641-6662, 2001.

[10] Kirsch, E., *Die Theorie der Elastizität und die Bedürfnisse der Festigkeitslehre*, Zeitschrift des Vereines deutscher Ingenieure, **42**, pp. 797-807, 1898.
[11] Liu, G.R. & Liu, M.B., *Smoothed Particle Hydrodynamics*, Singapore: World Scientific Printers Pte Ltd, 2003.
[12] Wiragunarsa, I.M., *Three Dimensional Elastodynamics and Fracture Mechanics Simulations using Smoothed Particle Hydrodynamics*, Institut Teknologi Bandung, Bandung, 2017.
[13] Humaedi, A., *Discretiation Correction of Particle Strength Exchange (DC PSE) Operator for 2D Steady State Incompressible Flow in Velocity Correction Scheme*, Institut Teknologi Bandung, Bandung, 2018.
[14] Sugandi, T.S., *2D Incompressible Flow Solver in Velocity-Vorticity Formulation Using DC-PSE Operator Discretization*, Institut Teknologi Bandung, Bandung, 2019.
[15] Tamai, T. & Koshizuka, S., *Least Square Moving Particle Semi-Implicit Method*, Comp. Part. Mech., pp. 277-305, 2014.